Electronic Supplementary Material (ESI) for Nanoscale.

Anisotropic shape of $CsPbBr_3$ colloidal nanocrystals: from 1D to 2D confinement effects

Violette Steinmetz[a], Julien Ramade[a], Laurent Legrand*[a], Thierry Barisien[a], Frédérick Bernardot[a], Emmanuel Lhuillier[a], Mathieu Bernard[a], Maxime Vabre[a], Imen Saïdi[b], Amal Ghribi[b], Kaïs Boujdaria[b], Christophe Testelin[a] and Maria Chamarro[a]

[a]Sorbonne Université, CNRS-UMR 7588, Institut des NanoSciences de Paris, INSP, 4 place Jussieu, F-75005, Paris, France.

[b]Laboratoire de Physique des Matériaux : Structure et Propriétés, Faculté des Sciences de Bizerte, Université de Carthage, 7021 Zarzouna, Bizerte, Tunisia

I. Chemical synthesis of $CsPbBr_3$ nanocrystals

I.1. Chemicals

Lead bromide ($PbBr_2$, > 98 % Aldrich), caesium carbonate (Cs_2CO_3, 99 %, Aldrich), lead acetate trihydrate ($Pb(CH_3COO)_2$.3H2O, 99 %, Aldrich), oleic acid (OA, 90 %, Aldrich), 1-octadecene (ODE, 90 %, Aldrich), oleylamine (OLA, 80-90 %, Acros Organics), ethylacetate (CH_3COOCH_3 , 99 %, Merck-Schuchardt), hydrobromic acid (HBr, 48 %), dimethylformamide (DMF, 99.8 %, Aldrich), acetone (VWR, 99.5 %).

I.2. Caesium oleate

In a three neck 50 mL flask, 350 mg of Cs_2CO_3 in 20 mL of ODE and 1.25 mL of OA are mixed. The flask is degassed under vacuum for the next 30 minutes at 110 ° C. The atmosphere is then switched to Ar and the temperature is raised to 150 ° C for 10 min. At this point the caesium salt is fully dissolved. The temperature is cooled down below 100 ° C and the flaks is further degassed for 10 min. The obtained gel is used as stock solution.

I.3. CsPbBr3 nanocrystals

Synthesis A of Nanosticks (NSTs): The nanosticks synthesis was carried out following reported synthesis protocol in [1] with one major modification. The reaction precursors and solvents were scaled up each by 8 times to improve yield and monodispersity of NPL thickness. 735 mg $PbBr_2$ are dissolved in 5 mL dimethylformamide in a 20 mL vial thanks to sonication. At room temperature and under ambient conditions 10 mL ODE, 1 mL OA, 1 mL OLA were taken in 250 ml flask and 0.8 mL of Cs (oleate) precursor was added under vigorous stirring. Then lead solution is injected and after 10 sec., nucleation of $CsPbBr_3$ nanocrystals was achieved by swiftly injecting 40 mL of acetone. The reaction contents were centrifuged at 6000 rpm and obtained pellet was redispersed in hexane.

Synthesis B of Nanoplatelets (NPLs): The nanoplatelets synthesis was carried out following reported synthesis protocol in [1] with one major modification. The reaction precursors and solvents were scaled up each by 8 times to improve yield and monodispersity of NPL thickness. 735 mg $PbBr_2$ are dissolved in 5 mL dimethylformamide in a 20 mL vial thanks to sonication. At room temperature and under ambient conditions 10 mL ODE, 1 mL OA, 1 mL OLA were taken in 250 ml flask, **with 240 μL of HBr** and 0.8 mL of Cs (oleate) precursor was added under vigorous stirring. Then lead solution is injected and after 10 sec., nucleation of $CsPbBr_3$ nanocrystals was achieved by swiftly injecting 40 mL of acetone. The reaction contents were centrifuged at 6000 rpm and obtained pellet was redispersed in hexane.

Name of the studied samples	Synthesis conditions (additive, solvent)
A1, A2, A3, A4	Synthesis A : 0 μL HBr, Hexane
B1, B2, B3	Synthesis B : 240 μL HBr, Hexane

TABLE I, SI: *Names and growth conditions of the studied samples. Samples have been obtained from hexane diluted solutions with different nanocrystal concentrations, as spin-coated or simply deposited drops on glass slides.*

II. Spectroscopic data on nanosticks sample

II.1. Attributions of a MLs number in a $CsPbBr_3$ nanostruture to the band-edge energies in absorption and luminescence from different groups

Assumed number of MLs: n =	11	10	9	8	7	6	5	4	3	2
E(eV) ABS, this work	2.385	2.405	2.425	2.46	2.505	2.575	2.695, 2.700	2.86, 2.90		
E(eV) PL, this work				2.47	2.515	2.585	2.70	2.90		
ref [1] (main text ref [27])							2.81	2.88	2.94	
ref [2] (main text ref [29])						2.572				
ref [3] (main text ref [30])						2.56	2.610	2.67	2.75	2.9
ref [4] (main text ref [26])						2.44				
ref [5] (main text ref [25])							2.577	2.61	2.73	2.87
PL, ref [6] (main text ref [28])						2.455	2.53	2.61	2.7	2.88
PL, ref [7] (main text ref [31])					2.42	2.445	2.485	2.555	2.655	

TABLE II, SI: *Experimental values of the band-edge energies versus the assumed numbers n of MLs of 0.58 nm. Data have been obtained mainly at room temperature from the absorption spectra.*

II.2. Temperature dependence of optical absorption and luminescence

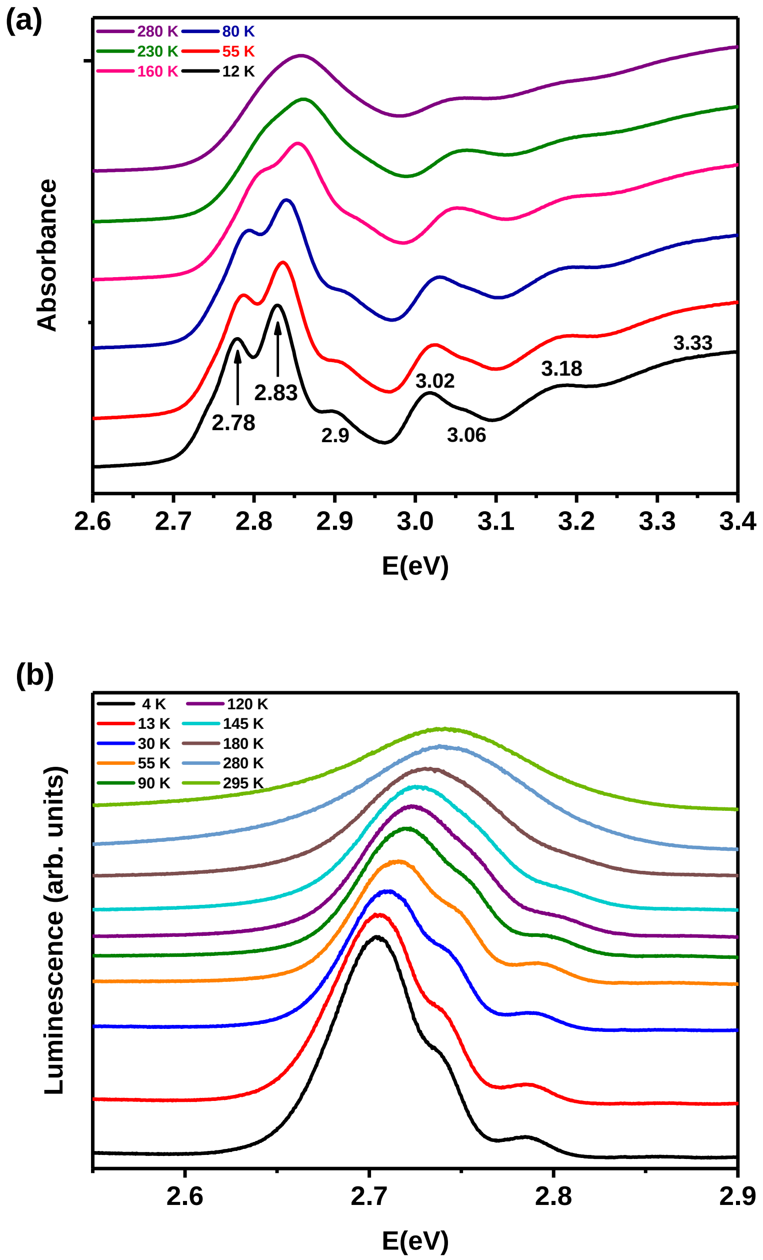

Fig. S. 1: Sample A2, **(a)** Temperature dependence of the absorption. **(b)** Emission as a function of temperature after laser excitation at 410 nm.

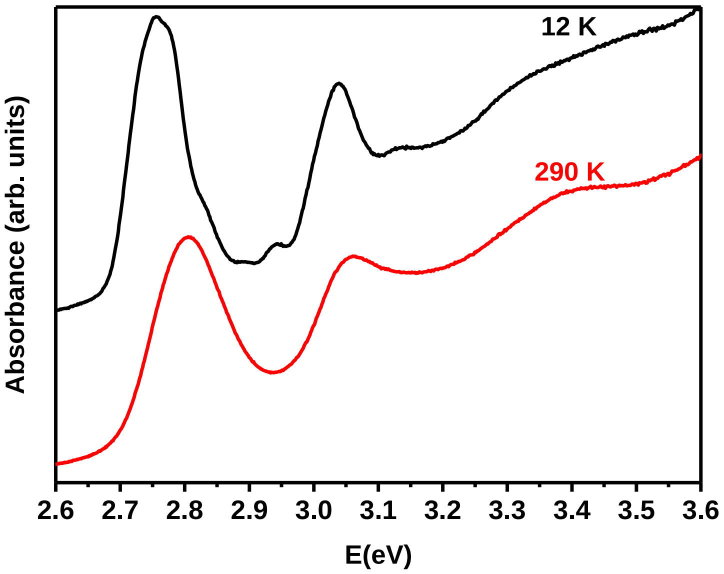

Fig. S. 2: Absorption at 12 K and close to room temperature as a function of temperature of sample A3.

II.3. Decomposition of the emission in Gaussian contributions

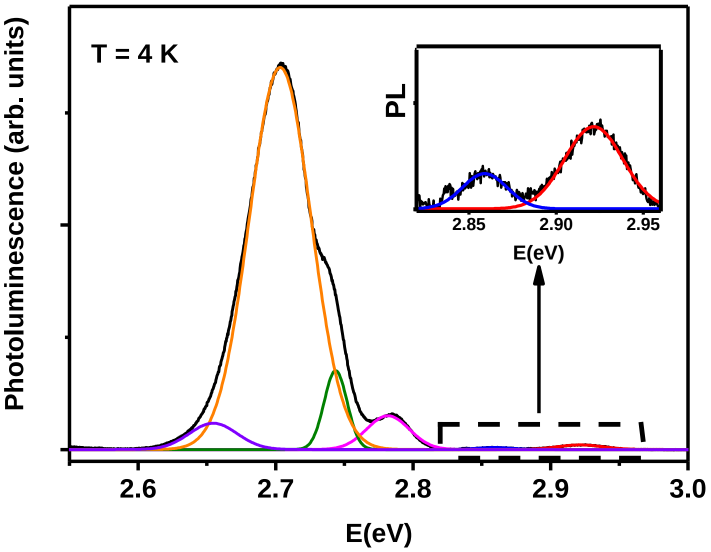

Fig. S. 3: Decomposition in 6 Gaussian contributions of the emission at 4 K of sample A2. Excitation is at 370 nm.

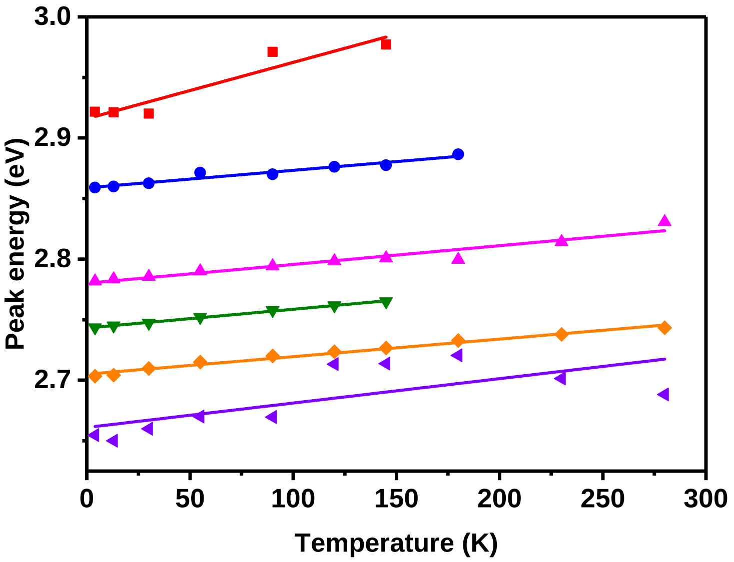

Fig. S. 4: Peak energies observed in Fig 3 SI as a function of temperature (sample A2). The colors code is the same as in Figs 3 SI.

II.4. Excitation power dependence of the emission

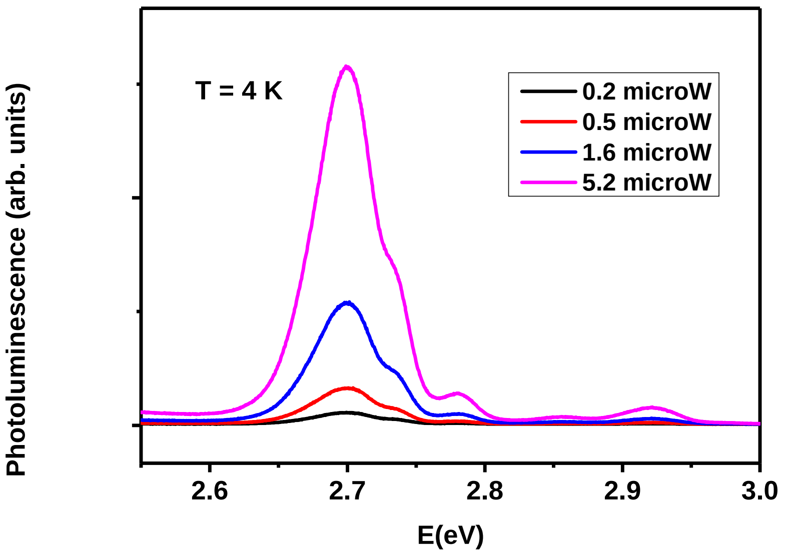

Fig. S. 5: Emission at 4 K of sample A2 as a function of the power of excitation at 370 nm.

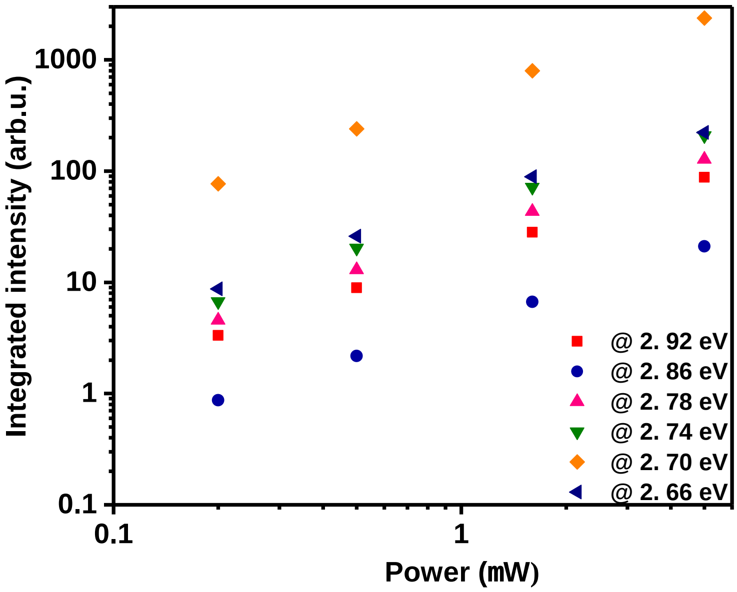

Fig. S. 6: Integrated intensity of the 6 Gaussian contributions of the emission spectra shown in Fig 5 SI as a function of the excitation power at 370 nm (sample A2). The colors code is the same as in Figs S.3 and S.4.

III. Theoretical support

III.1. Multiband k.p model for O$_h$ semiconductors

In the framework of the **k.p** theory, we develop a 40-band model in cubic phase perovskites for which the point symmetry group is O_h. For the clarity of the analysis, we begin by introducing the procedure followed to build the Hamiltonian used in this work.

III.1.1. Symmetry considerations

The present model involves both valence- and conduction bands having s, p, and d symmetries. Based on the character table of O$_h$ group, which is given explicitly in Table III, one can deduce

$$\begin{cases} s_V \sim \Gamma_1^+ \ (\Gamma_6^+) & , \quad s_C \sim \Gamma_2^- \ (\Gamma_7^-) \\ p_V \sim \Gamma_5^+ \ (\Gamma_7^+ + \Gamma_8^+) & , \quad p_C \sim \Gamma_4^- \ (\Gamma_6^- + \Gamma_8^-) \\ d_V \sim \Gamma_3^+ \ (\Gamma_{(8-3)}^+) & , \quad d_C \sim \Gamma_3^- \ (\Gamma_{(8-3)}^-) \end{cases} \tag{1}$$

in which the subscript C(V) indicates the conduction band (CB) (valence band (VB)). The symbol " $\sim$ " points out how the CB and VB states transform under O$_h$ operations. Γ_n^α (Γ_m^β) indicate the single-group (double-group) representations of O$_h$ group. In Fig. S. 7, we represent schematically the model and indicate the corresponding states to the bands involved in the present modelization. Under O$_h$ operations, we have $(|X_{dC}\rangle, |Y_{dC}\rangle, |Z_{dC}\rangle) \sim \Gamma_{5d}^+$, $(|D_{zC}\rangle, |D_{xC}\rangle) \sim \Gamma_{3d}^-$, $(|X_{dV}\rangle, |Y_{dV}\rangle, |Z_{dV}\rangle) \sim \Gamma_{4d}^-$, $(|D_{zV}\rangle, |D_{xV}\rangle) \sim \Gamma_{3d}^+$, $(|X_C\rangle, |Y_C\rangle, |Z_C\rangle) \sim \Gamma_{4C}^-$, $(|X_V\rangle, |Y_V\rangle, |Z_V\rangle) \sim \Gamma_5^+$, $|S_C\rangle \sim \Gamma_2^-$, $|S_V\rangle \sim \Gamma_1^+$, $|S_u\rangle \sim \Gamma_{1U}^+$, and $|S_q\rangle \sim \Gamma_{2U}^-$.

O_h	E	$8C_3$	$6C_2$	$6C_4$	$3C_2$	i	$6S_4$	$8S_6$	$3\sigma_h$	$6\sigma_d$	Basis
Γ_1^+	1	1	1	1	1	1	1	1	1	1	$x^2+y^2+z^2=r^2$
Γ_2^+	1	1	-1	-1	1	1	-1	1	1	-1	$f_2^+ = (x^2-y^2)(y^2-z^2)(z^2-x^2)$
Γ_3^+	2	-1	0	0	2	2	0	-1	2	0	$D_z = (3z^2-r^2)\,, D_x = \sqrt{3}(x^2-y^2)$
Γ_4^+	3	0	-1	1	-1	3	1	0	-1	-1	$\mathcal{R}_x, \mathcal{R}_y, \mathcal{R}_z$
Γ_5^+	3	0	1	-1	-1	3	-1	0	-1	1	yz, zx, xy
Γ_1^-	1	1	1	1	1	-1	-1	-1	-1	-1	$f_2^+ \times xyz$
Γ_2^-	1	1	-1	-1	1	-1	1	-1	-1	1	xyz
Γ_3^-	2	-1	0	0	2	-2	0	1	-2	0	$xyz \times D_z, xyz \times D_x$
Γ_4^-	3	0	-1	1	-1	-3	-1	0	1	1	x, y, z
Γ_5^-	3	0	1	-1	-1	-3	1	0	1	-1	$f_2^+ \times xyz \times yz$ $f_2^+ \times xyz \times zx$ $f_2^+ \times xyz \times xy$

TABLE III, SI: *Character table of group O_h and the basis functions for each irreducible representation. Here (x,y,z) are the three Cartesian components of an ordinary vector and ($\mathcal{R}_x, \mathcal{R}_y, \mathcal{R}_z$) are the three Cartesian components of an axial vector.*

III.1.2. Modeling electronic structure

In cubic symmetry, we are in no-crystal-field case. As a result, to solve the electronic Schrödinger equation in cubic phase perovskites, we use the following Hamiltonian

$$\mathcal{H} = \mathcal{H}_0 + \mathcal{H}_{\mathbf{k.p}} + \mathcal{H}_{\mathbf{so}} \tag{2}$$

where

$$\begin{cases} \mathcal{H}_0 = \frac{P^2}{2m_0} + \mathcal{U} + \frac{\hbar^2 k^2}{2m_0} \\ \mathcal{H}_{\mathbf{k.p}} = \frac{\hbar}{m_0}\mathbf{k.p} \\ \mathcal{H}_{\mathbf{so}} = \xi \mathcal{G}.\sigma \end{cases} \tag{3}$$

Here m_0 is the free electron mass, and $\mathcal{U}$ is a potential having the lattice periodicity, $\mathcal{G} = (\nabla \mathcal{U} \times \mathbf{p})$ is the spin-orbit operator, $\sigma = (\sigma_x, \sigma_y, \sigma_z)$ are the Pauli spin matrices and $\xi = \hbar/4m_0^2c^2$.

Under O$_h$ operations, $\mathcal{H}_0$ transforms like Γ_1^+ which is the unit representation of O$_h$ group. The coupling terms via $\mathcal{H}_0$ occur between the same levels, so that the matrix blocks corresponding to $\mathcal{H}_0$ are $\left(E_{\Gamma_m^\epsilon} + \frac{\hbar^2 k^2}{2m_0}\right)\mathcal{I}$, where $\mathcal{I}$ is the unit matrix of the representation dimension.

Once $\mathcal{H}_0$ matrix representation is obtained, we then derive the nonzero matrix elements of $\mathcal{H}_{\mathbf{k.p}}$ and $\mathcal{H}_{\mathbf{so}}$. They are obtained according to the following rule: the matrix elements of a given operator $\mathcal{O}$, namely $\langle \chi_n^\alpha | \, \mathcal{O} \, | \phi_p^\eta \rangle$, is nonzero when the product $\Gamma_n^\alpha \otimes \Gamma_m^\epsilon \otimes \Gamma_p^\eta$ contains the unit representation (that is Γ_1^+ in O_h group); here $|\chi_n^\alpha\rangle$ $\big(\mathcal{O}$ and $|\phi_p^\eta\rangle\big)$ is of Γ_n^α symmetry $\big($respectively Γ_m^ϵ and $\Gamma_p^\eta\big)$ $(\alpha = \pm, \epsilon = \pm, \eta = \pm)$.

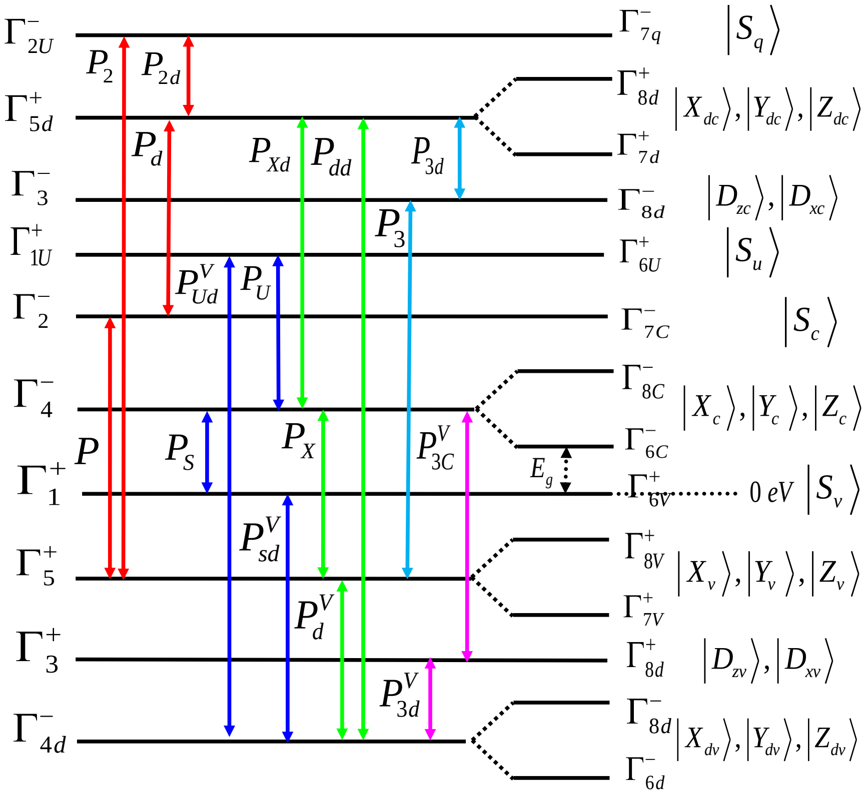

Fig. S. 7: Schematic illustration of the 40-band **k.p** model, the symmetries of the involved bands and momentum matrix elements are represented.

III.1.2.1. $H_{\mathbf{k.p}}$ matrix elements

It is well known that the momentum $\mathbf{p}$ is an ordinary vector, hence $(p_x, p_y, p_z) \sim (x, y, z)$ and according to Table III, the operator $\mathbf{p}$ transforms like Γ_4^- in the O_h symmetry group. One obtains 16 nonzero **k.p** matrix elements that we have classified as follows:

- Four coupling terms appear between the states having a Γ_2^- and Γ_5^+ symmetry, namely $P = (\hbar/m_0)\langle S_C| p_x |iX_V\rangle$, $P_2 = (\hbar/m_0)\langle S_q| p_x |iX_V\rangle$, $P_d = (\hbar/m_0)\langle S_C| p_x |iX_{dC}\rangle$, and $P_{2d} = (\hbar/m_0)\langle S_q| p_x |iX_{dC}\rangle$.

- Four **k.p** matrix elements depicting the coupling between the states of Γ_1^+ and Γ_4^- symmetry, denoted by $P_S = (\hbar/m_0)\langle S_V| p_x |iX_C\rangle$, $P_U = (\hbar/m_0)\langle S_u| p_x |iX_C\rangle$, $P_{Sd}^V = (\hbar/m_0)\langle S_V| p_x |iX_{dV}\rangle$, and $P_{Ud}^V = (\hbar/m_0)\langle S_u| p_x |iX_{dV}\rangle$.

- Four **k.p** matrix elements resulting from the coupling between the states having a Γ_5^+ and Γ_4^- symmetry, namely $P_X = (\hbar/m_0)\langle X_V|\, p_y\, |iZ_C\rangle$, $P_{Xd} = (\hbar/m_0)\langle X_C|\, p_y\, |iZ_{dC}\rangle$, $P_d^V = (\hbar/m_0)\langle X_V|\, p_y\, |iZ_{dV}\rangle$, and $P_{dd} = (\hbar/m_0)\langle X_{dC}|\, p_y\, |iZ_{dV}\rangle$.

- Two coupling terms appear between the states of Γ_3^- and Γ_5^+ symmetry, denoted by $P_3 = \langle iX_V|\, p_x\, |D_{zC}\rangle$ and $P_{3d} = \langle iX_{dC}|\, p_x\, |D_{zC}\rangle$.

- Two **k.p** matrix elements describing the coupling between the states having a Γ_4^- and Γ_3^+ symmetry, namely $P_{3d}^V = \langle iX_{dV}|\, p_x\, |D_{zV}\rangle$ and $P_{3C}^V = \langle iX_C|\, p_x\, |D_{zV}\rangle$.

The entirely of these matrix elements are real-valued and considered as adjustable parameters. The energies related to the interband momentum matrix elements, P_j, are defined as $E_{P_j} = (2m_0/\hbar^2)\, P_j^2$. We summarize in Fig. S. 7 all the **k.p** matrix elements involved in this model.

The second-order terms of k, induced by the $\mathcal{H}_{\mathbf{k.p}}$ Hamiltonian, are also considered in the present approach. Adopting similar method to that of the Luttinger-Kohn paper [8], we obtain four matrix blocks describing the second-order corrections. One find them inside Γ_5^+ $(\Gamma_{7V}^+ + \Gamma_{8V}^+)$ VBs, Γ_{4d}^- $(\Gamma_{6d}^- + \Gamma_{8d}^-))$ VBs, Γ_4^- $(\Gamma_{6C}^- + \Gamma_{8C}^-)$ CBs, and Γ_{5d}^+ $(\Gamma_{7d}^+ + \Gamma_{8d}^+))$ CBs. Formally, all these blocks-matrix have the same structure, for example the ones inside the Γ_5^+ VBs or Γ_4^- CBs are given explicitly in Ref. [9].

III.1.2.2. Spin-orbit coupling

Let us now add spin and consider spin-orbit interaction effect into analysis. After neglecting the k-dependent spin-orbit term, namely $\hbar^2/4m_0^2c^2\ (\nabla\mathcal{U}\times\mathbf{k}).\sigma$, we can modeled the spin-orbit Hamiltonian as $\mathcal{H}_{\mathbf{so}} = \xi\mathcal{G}.\sigma$. $\mathcal{G}$ being an axial vector, we have $(\mathcal{G}_x, \mathcal{G}_y, \mathcal{G}_z) \sim (\mathcal{R}_x, \mathcal{R}_y, \mathcal{R}_z)$, hence the operator $\mathcal{G}$ transforms such as Γ_4^+ under the O_h operations. Ten spin-orbit interaction terms are obtained and listed according to Bloch states symmetries, as follows

- Three coupling terms appear inside the p-like states in the CB and VB having a Γ_5^+ symmetry, namely $\Delta = 3\xi\langle X_V|\, \mathcal{G}_z\, |iY_V\rangle$, $\Delta_d = 3\xi\langle X_{dC}|\, \mathcal{G}_z\, |iY_{dC}\rangle$, and $\Delta_{dso} = 3\xi\langle X_V|\, \mathcal{G}_z\, |iY_{dC}\rangle$.

- Three coupling terms appear inside the p-like states in the CB and VB having a Γ_4^- symmetry, denoted by $\Delta_C = 3\xi\langle X_C|\, \mathcal{G}_z\, |iY_C\rangle$, $\Delta_d^V = 3\xi\langle X_{dV}|\, \mathcal{G}_z\, |iY_{dV}\rangle$, and $\Delta_{Cd}^V = 3\xi\langle X_{dV}|\, \mathcal{G}_z\, |iY_C\rangle$.

- Two coupling terms appear between the d-like states in the CB with a Γ_3^- symmetry and p-like states in the CB or VB having a Γ_4^- symmetry, denoted by $\Delta_{3C} = 2\sqrt{2}\xi \left\langle D_{zC} \right| \mathcal{G}_x \left| iX_C \right\rangle$ and $\Delta_{3d}^V = 2\sqrt{2}\xi \left\langle iX_{dV} \right| \mathcal{G}_x \left| D_{zC} \right\rangle$.

- Two coupling terms appear between the d-like states in the VB with a Γ_3^+ symmetry and p-like states in the CB or VB having a Γ_5^+ symmetry, namely $\Delta_3^V = 2\sqrt{2}\xi \left\langle D_{zV} \right| \mathcal{G}_x \left| iX_V \right\rangle$ and $\Delta_{3dd}^V = 2\sqrt{2}\xi \left\langle D_{zV} \right| \mathcal{G}_x \left| iX_{dC} \right\rangle$.

The totality of the nonzero spin-orbit coupling terms are summarized in Fig. S. 8.

We derive the matrix representation of $\mathcal{H}$ after having projected the total Hamiltonian on a finite basis, whose expression is given explicitly in Ref. [10]. We now apply the model to calculate the band structure (BS) of bulk perovskites, CsPbX$_3$ ($X = I$, Br, Cl).

III.2. Electronic properties

We begin our analysis by describing our strategy to optimize the **k.p** parameters needed to accurately reproduce the band diagram of bulk inorganic perovskite compounds, CsPbX$_3$. Numerically, we differentiate two types of input parameters. The first ones are taken as adjustable parameters such as $\left(E_P, E_{P_S}, E_{P_X}, E_{P_d}, E_{P_{Xd}}, E_{P_U}, E_{P_{3C}^V}, E_{P_{sd}^V}, \Delta, \Delta_C\right)$. They are optimized so that our band diagram results match well the predictions of others authors [11, 12] who adopt calculations based on the density functional theory (DFT). The rest of input parameters, namely $\left(E_{P_2}, E_{P_{2d}}, E_{P_{dd}}, E_{P_3}, E_{P_{3d}}, E_{P_d^V}, E_{P_{Ud}^V}, E_{P_{3d}^V}, \Delta_{3dd}^V, \Delta_{3d}^V, \Delta_{3C}, \Delta_{cd}^V, \Delta_{dso}\right)$, were intentionally taken null due to their smaller impact on CB an VB dispersions.

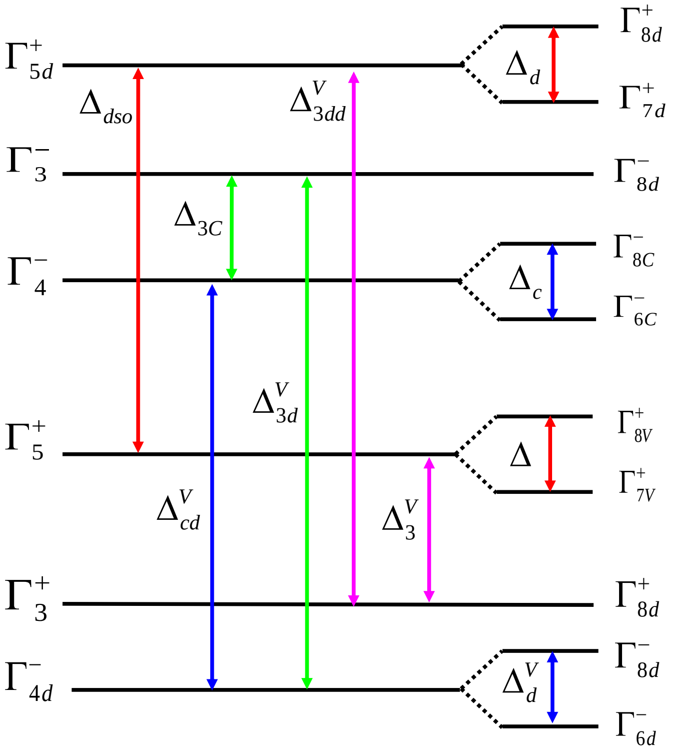

Fig. S. 8: Effect of spin-orbit interaction within the 40-band **k.p** model.

III.2.1. Band diagram

To establish the validity of the present model, we compare our results with the ones available in the literature. In Fig. S. 9, we show the BS of cubic CsPbX$_3$ (X = I, Br, Cl) simulated with the present 40-band **k.p** model. We can see that the conduction and valence band edges are located at the point $R = \frac{\pi}{a}(1,1,1)$ of the Brillouin zone and the three materials have a direct band gap characters. The BS is given on a width of about 8 eV: the VB over a 4 eV scale and the lowest CBs over a 4 eV scale over a wide range of k-vectors along four directions (RM, $R\Gamma$, MX, ΓX). Surroundings the R point, a quasi-isotropic energy dispersion of the upper VB and the lowest split-off CB is observed. Numerical values listed in Table IV outline the comparison of our results to those predicted from

DFT calculations [11–13], or with the available experimental data given by Yang et al [14]. We obtain comparable magnitudes of the band-edge energies for the three materials. A satisfying agreement is clearly obtained between the two approaches along the RM direction for CsPbI$_3$ and CsPbBr$_3$ (see the values of M_6^- and M_6^+ in Table IV). The consistency of the two approaches is also obtained along $R\Gamma$ direction, in particular for CsPbCl$_3$ and CsPbBr$_3$ (see the values of Γ_6^- in Table IV). However, differences appear between our results and the ones of others authors [11–13] for the upper VB along $R\Gamma$ direction (see the values of Γ_6^+ in Table IV). In part, this discrepancy might originate from missing interactions, especially with the remote bands (mainly the f levels), which are not considered within the 40-band **k.p** model. Moreover, the adopted values of the band parameters across the literature having controversial estimations can explain such discrepancies. Note also that our predictions on the band dispersions for both second CB and second VB clearly deviate with the ones obtained by DFT calculations [11, 12].

The bandgap E_g is adjusted to achieve best fit to the experimental data of Ref. [14]. One gets 1.74, 2.37 and 2.70 eV for CsPbX$_3$ ($X = I, Br, Cl$), respectively. These values are in line with previous estimations given in Ref. [12] and one observe a disagreement smaller than 12% in the worst case (CsPbCl$_3$). In the case of CsPbBr$_3$, our E$_g$ value agrees very well with the value $E_g = 2.454$ eV derived from recent DFT calculations [15]. The spin-orbit coupling parameters is also evaluated and we obtain higher values as compared to the more familiar III-V and II-VI semiconductors: 1.30 eV for CsPbI$_3$, 1.39 eV for CsPbBr$_3$, and 1.58 eV for CsPbCl$_3$. Our predictions are in line with the data available in the literature, namely 1.55 eV for CsPbI$_3$ and 1.543 eV for CsPbBr$_3$ obtained from DFT calculations [15]. Once we have validated the (E_g, Δ_C) estimations, we focus on the Kane energy $E_{P_S} = (2m_0/\hbar^2)\, P_S^2$. Our resulting estimates of E_{P_S} range from 24 eV to 30 eV which are slightly lower than theoretical results given in Refs. [11, 12]. In the case of CsPbBr$_3$, our value of $E_{P_S} = 28.41$ eV agrees very well with the value $E_{P_S} = 27.88$ eV derived from DFT calculations [15].

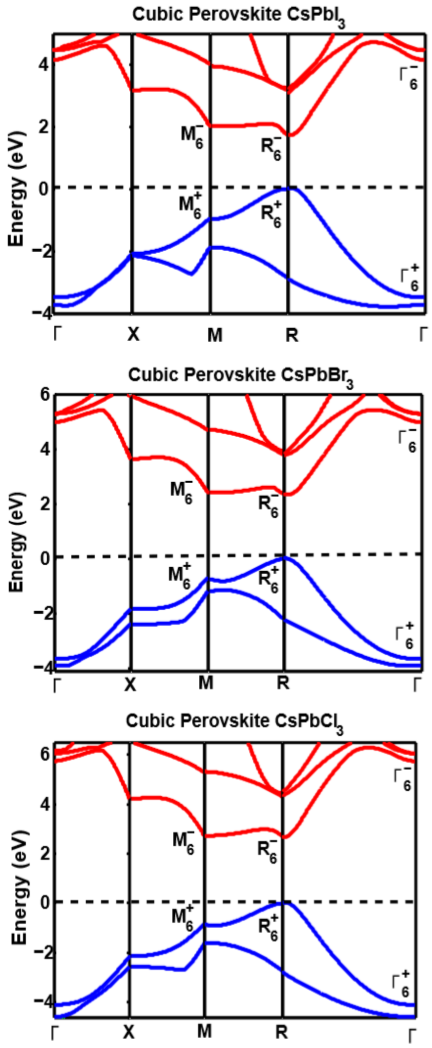

Fig. S. 9: Energy band structure of bulk $CsPbX_3$ (X=I, Br, Cl) obtained from the 40-band **k.p** model.

III.2.2. Basic physical parameters

We test our estimations of the reduced exciton effective mass, μ, and the exciton binding energy, E_X, against the results reported in the literature. The values of the carrier effective masses, (m_e, m_h), extracted from the present **k.p** model are summarized in Table V. In these last predictions, we use the following relationships:

eV	CsPbI$_3$				CsPbBr$_3$				CsPbCl$_3$		
Reference	[12]	[11, 13]	Exp [14]	**k.p**	[12]	[11, 13]	Exp [14]	**k.p**	[12]	[11, 13]	**k.p**
Γ_6^-	4.4	4.77		4.15	4.71	5.11		4.97	5.60	5.55	5.74
Γ_6^+	-1.6	-1.66		-3.48	-2.5	-2.45		-3.66	-3	-3.11	-4.10
M_6^-	2.55	2.5		2.02	3.43	3.33		2.41	4.03	3.88	2.74
M_6^+	-0.55	-0.6		-0.96	-0.86	-0.88		-0.74	-0.88	-1	-0.86
$E_g(R_6^-)$	1.67	1.44	1.72	1.74	2.36	2	2.34	2.37	3.04	2.82	2.70
E_{P_s}	41.6	34.72	7.56	23.81	39.9	37.19	9.29	28.41	40.10	37.19	29.81

TABLE IV, SI: *Electronic structure parameters obtained from the 40-band k.p model and their comparison with the available data given in the literature.*

$$\frac{m_0}{m_h} = -1+\frac{E_{P_s}}{3}\left[\frac{2}{\left(E_{\Gamma^-_{8C}}-E_{\Gamma^+_{6V}}\right)}+\frac{1}{\left(E_{\Gamma^-_{6C}}-E_{\Gamma^+_{6V}}\right)}\right]+\frac{E_{P^V_{sd}}}{3}\left[\frac{2}{\left(E_{\Gamma^+_{6V}}-E_{\Gamma^-_{8d}}\right)}+\frac{1}{\left(E_{\Gamma^+_{6V}}-E_{\Gamma^-_{6d}}\right)}\right] \quad (4)$$

and

$$\frac{m_0}{m_e} = 1+\frac{2}{3}\frac{E_{P_X}}{\left(E_{\Gamma^-_{6C}}-E_{\Gamma^+_{8V}}\right)}+\frac{1}{3}\frac{E_{P_S}}{\left(E_{\Gamma^-_{6C}}-E_{\Gamma^+_{6V}}\right)}+\frac{2}{3}\frac{E_{P_{Xd}}}{\left(E_{\Gamma^-_{6C}}-E_{\Gamma^+_{8d}}\right)}+\frac{1}{3}\frac{E_{P_U}}{\left(E_{\Gamma^-_{6C}}-E_{\Gamma^+_{6U}}\right)}+\frac{4}{3}\frac{E_{P^V_{3C}}}{\left(E_{\Gamma^-_{6C}}-E_{\Gamma^+_{(8-3)d}}\right)} \quad (5)$$

We use the (m_e, m_h) values given in Table V to deduce the reduced exciton effective mass $\mu^{-1} = m_e^{-1} + m_h^{-1}$, one get 0.104 m_0/0.117 m_0/0.13 m_0 for CsPbI$_3$/CsPbBr$_3$/CsPbCl$_3$ which are consistent with the experimental results given in Ref. [14]. Our predictions are significantly larger than early estimates obtained from DFT calculations [11, 12] especially for CsPbI$_3$ and CsPbBr$_3$. Note that, in the case of CsPbBr$_3$, our μ value is in line with 0.132m_0 value predicted by Sercel et al [15]. The last parameter needed to estimate E_X is the relative dielectric constant, ϵ_r. The approach detailed in Ref. [16] allows us to calculate ϵ_r, one get $\epsilon_r = 9.13$ for CsPbI$_3$, 7.08 for CsPbBr$_3$ and 5.45 for CsPbCl$_3$ which are in good agreement with the available experimental data [14]. However, the present model predicts the ϵ_r values slightly greater than the ones determined by DFT calculations [11, 12]. Having determined $(\mu(m_0), \epsilon_r)$, we can estimated the exciton binding energy from the relationship $E_X = (\mu e^4/8\epsilon_0^2\epsilon_r^2h^2)$. We get 16.98 meV for CsPbI$_3$ and 31.76 meV for CsPbBr$_3$ which are very close to those given in Ref. [14]. Moreover, in the case of CsPbBr$_3$, our prediction is very close to that calculated by DFT [15], $E_X = 33.7$ meV. For CsPbCl$_3$, and from the couple $(\mu(m_0), \epsilon_r) = (0.130, 5.45)$, we get $E_X = 59.55$ meV which agrees very well with the experimental values of 60 meV given in Ref. [17] and 67 meV given in Ref. [18]. The present model predicts basic physical parameters that are in good agreement with experiment.

	CsPbI$_3$				CsPbBr$_3$				CsPbCl$_3$		
Reference	[12]	[11, 13]	Exp [14]	**k.p**	[12]	[11, 13]	Exp [14]	**k.p**	[12]	[11, 13]	**k.p**
E_{P_s}	41.6	34.72	7.56	23.81	39.9	37.19	9.29	28.41	40.10	37.19	29.81
E_g	1.67	1.44	1.72	1.74	2.36	2	2.34	2.37	3.04	2.82	2.70
m_e (m_0)	0.086	0.11		0.279	0.134	0.15		0.308	0.194	0.2	0.319
m_h (m_0)	0.095	0.13		0.165	0.128	0.14		0.188	0.17	0.17	0.219
μ (m_0)	0.045	0.059	0.114	0.104	0.065	0.072	0.126	0.117	0.091	0.1	0.130
ϵ_r	5	6.32	10	9.13	4.8	4.96	7.3	7.08	4.5	4.07	5.45
E_X (meV)	24.48	20.09	15	16.98	38.37	39.8	33	31.76	61.12	82.1	59.55

TABLE V, SI: *Parameters determined from the 40-band k.p model and their comparison with the available data given in the literature.*

---

[1] Q. A. Akkerman, S. Genaro Motti, A.R. S. Kandada, E. Mosconi, V. D'Innocenzo, G. Bertoni, S. Marras, B.A. Kamino, L. Miranda, F. De Angelis, A. Petrozza, M. Prato and L. Manna, J. Am. Chem. Soc. **138**, 1010-1016 (2016).

[2] F. Bertolotti, G. Nedelcu, A. Vivani, A. Cervellino, N. Masciocchi, A. Guagliardi and M. V. Kovalenko, ACS Nano **13**, 14294-14307 (2019).

[3] J. B. Bohn, Y. Tong, M. Gramlich, M. L. Lai, M. Doblinger, K. Wanf, R. L. Z. Hoye, P. Müller-Buschbaum, S. D. Stranks, A. S. Urban, L. Polavarapu and J. Feldmann, Nano Lett. **18**, 5231-5238 (2018).

[4] S. Sun, D. Yuan, Y. Xu, A. Wang and Z. Deng, ACS Nano, **10**, 3648-3657 (2016).

[5] Y. Bekenstein, B. A. Koscher, S. W. Eaton, P. Yang and A. P. Alivisatos, J. Am. Chem. Soc. **137**, 16008-16011 (2015).

[6] J. Cho, H. Jin, D.G. Sellers, D. F. Watson, D. H. Son and S. Banerjee, J. of Materials Chemistry C **5**, 8810-8818 (2017).

[7] C. Huo, Ch.F. Fong, M-R Amara, Y. Juang, B. Chen, J. Zhang, L. Guo, H. Li, W. Juang, C. Diederichs and Q. Xiong, Nano Lett., https://dx.doi.org/10.1021/acs.nanolett.0c00611

[8] J. M. Luttinger and W. Kohn, Phys. Rev. **97**, 869 (1955).

[9] S. Ridene, K. Boujdaria, H. Bouchriha, and G. Fishman, Phys. Rev. B **64**, 085329 (2011).

[10] R. Neffati, I. Saïdi, and K. Boujdaria, J. Appl. Phys. **112**, 053716 (2012).

[11] L. Protesescu, S. Yakunin, M. I. Bodnarchuk, F. Krieg, R. Caputo, C. H. Hendon, R. Xi. Yang, A. Walsh, and M. V. Kovalenko, Nano. Lett. **15**, 3692 (2015).

[12] M. A. Becker, R. Vaxenburg, G. Nedelcu, P. C. Sercel, A. Shabaev, M. J. Mehl, J. G. Michopoulos, S. G. Lambrakos, N. Bernstein, J. L. Lyons, T. Stöferle, R. F. Mahrt, M. V. Kovalenko, D. J. Norris, G. Rainò, and A. L. Efros, Nature **553**, 189 (2018).

[13] M. O. Nestoklon, S. V. Goupalov, R. I. Dzhioev, O. S. Ken, V. L. Korenev, Yu. G. Kusrayev, V. F. Sapega, C. de Weerd, L. Gomez, T. Gregorkiewicz, J. Lin, K. Suenage, Y. Fujiwara, L. B. Matyushkin, and I. N. Yassievich, Phys. Rev. B **97**, 235304 (2018).

[14] Z. Yang, A. Surrente, K. Galkowski, A. Miyata, R. J. Sutton, A. A. Haghighirad, H. J. Snaith, D. K. Maude, P. Plochocka, and R. J. Nicholas, ACS Energy Lett. **2**, 1621 (2017).

[15] P. C. Sercel, J. L. Lyons, N. Bernstein, and A. L. Efros, J. Chem. Phys. **151**, 234106 (2019).

[16] M. Yahyaoui, H. Riahi, M. A. Maaref, K. Boujdaria, A. Lemaître, L. Thevenard, and C. Gourdon, J. Appl. Phys. **121**, 125702 (2017).

[17] I. P. Pazhuk, N. S. Pydzirailo, and M. G. Matsko, Sov. Phys. Sol. State 23, 1263 (1981).

[18] D. Fröhlich, K. Heidrich, H. Künzel, G. Trendel, and J. Treusch, Journal of Luminesence **18/19**, 385 (1979).